



Fault zone damage caused by the mainshock rupture during the 2014 Northern Nagano earthquake



Titouan Muzellec^{1,2}, Grazia De Landro¹ & Aldo Zollo¹

Seismic velocity variations before and after major earthquakes, measured with ambient noise interferometry, reveal time-dependent changes in subsurface properties, but the physical mechanism that causes them remains difficult to identify. Using noise interferometry, we observed a 0.5–1.3% velocity reduction within the upper-crust where the Mw 6.2 Northern Nagano earthquake rupture reached the surface. We combined the inverted 2D image with depth sensitivity to reconstruct the distribution of velocity changes in the shallow crust and show its correlation with the surface rupture and high-slip zones. Our results suggest that the main cause of velocity drop in the first kilometers of depth is damage induced by the mainshock rupture. Both fault-zone damage and near-surface damage from strong ground-shaking are involved, supported by the spatial correlation of velocity perturbations with peak ground acceleration and coseismic slip. These findings highlight fault zone weakening and shaking-induced damage as key drivers of post-earthquake velocity variations.

Temporal changes in crustal seismic velocity are often attributed to stress variations and damage/recovery processes. They have been observed in the fault embedding volume following large earthquakes, indicating a characteristic mechanical behavior of the medium^{1,2}.

Ambient seismic noise is increasingly employed to track velocity changes in the shallow crust of tectonic/volcanic regions using seismic noise cross-correlation³, a technique that does not depend on the earthquake occurrences. Several studies have used ambient noise interferometry to detect small velocity variations, less than 1%, in association with large earthquakes^{1,4,5} and volcanic activity^{6–8} or to monitor seasonal seismic velocity variations induced by changes in ground-water level^{9–13}. In these scenarios, several mechanisms contribute to seismic velocity changes, including variations in crustal stress condition^{14–17}, rock damage caused by strong ground shaking^{5,18,19}, healing of the fault interface and surrounding volume^{1,20,21} or pore pressure changes related to fluid presence/migration^{11,22}.

Although the temporal evolution of velocity in the epicentral volume of large earthquakes have been investigated^{1,2,4,5,15}, discriminating the relative contributions of the causative mechanisms remains a significant challenge^{23,24}.

To better understand the mechanisms driving velocity variations, it is essential to accurately locate the perturbations both horizontally and with depth, enabling their spatial correlation with the mainshock location^{20,25}. Furthermore, comparing the velocity change amplitudes from cross-

correlation and auto-correlation methods provides insight into the depth distribution of these changes²⁶. Moreover, combining this observation with the analysis of other geophysical parameters, sensitive to the mechanical state of the medium (e.g., peak ground acceleration, stress changes, ...) is crucial to identify the mechanisms responsible for the observed velocity changes^{5,10,27,28}.

In this study, we revealed the temporal and spatial variations of seismic velocity associated with the Mw 6.2 2014 Northern Nagano earthquake. We focus our study on the Nagano earthquake due to a combination of observational and seismotectonic factors that make it a particularly suitable case for investigating shallow co-seismic velocity changes. The Mw 6.2 earthquake, occurred on 22 November 2014, near the Kamishiro fault (KF) and Otari-Nakayama fault (OTNF) (cyan star in Fig. 1) along the Itoigawa-Shizuoka Tectonic Line (ISTL), one of the most active intraplate fault systems in Japan. KF and OTNF are the boundaries of the Northern Fossa Magna (NFM) rift basin in the East and older basement rocks of the “Inner zone” (INZ) in the West. The earthquake was originated by a SW-NE trending and SE dipping reverse fault rupture mechanism with a left-lateral component^{29,30}. The Nagano earthquake generated clear surface faulting over approximately 9 km along the KF, with local displacements up to 1 meter³¹. Despite its moderate magnitude, the earthquake caused notable infrastructural damage and activated a complex multi-segmented fault system accompanied by a rich aftershock sequence exceeding 2500 events. The region is also covered by a dense seismic network, enabling high-

¹Dipartimento di Fisica E. Pancini, Università degli Studi di Napoli “Federico II”, RISSC-Lab, Naples, Italy. ²Department of Meteorology and Geophysics, University of Vienna, Vienna, Austria. e-mail: grazia.delandro@unina.it

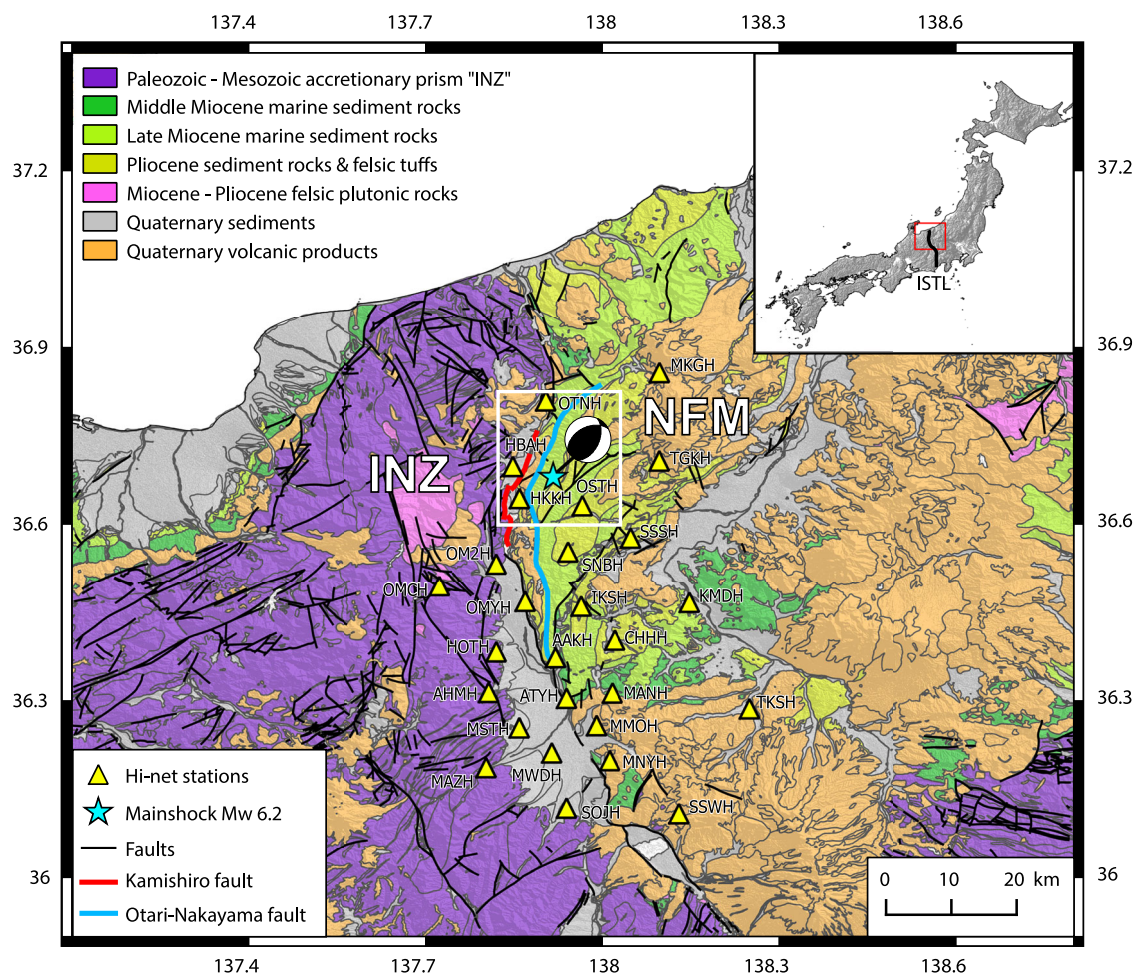


Fig. 1 | Map view of the geological structures in the study area of the 2014 Nagano earthquake sequence. The cyan star indicates the M_w 6.2 mainshock location. Yellow triangles indicate the locations of the seismic stations used in this study. The red and blue lines on the map correspond to the fault traces at the surface of the

Kamishiro fault and the Otari-Nakayama fault respectively. NFM Northern Fossa Magna, INZ Inner Zone, ISTL Itoigawa-Shizuoka tectonic line. Faults and geological units from GSJ-AIST (2025, CC BY 4.0); topography from GSI DEM10B (OGL-Japan).

resolution ambient noise interferometry and precise localization of velocity changes. These conditions allow us to link interferometric observations with independently mapped rupture features and assess the distribution of shallow co-seismic damage with a level of spatial detail that is rarely achievable.

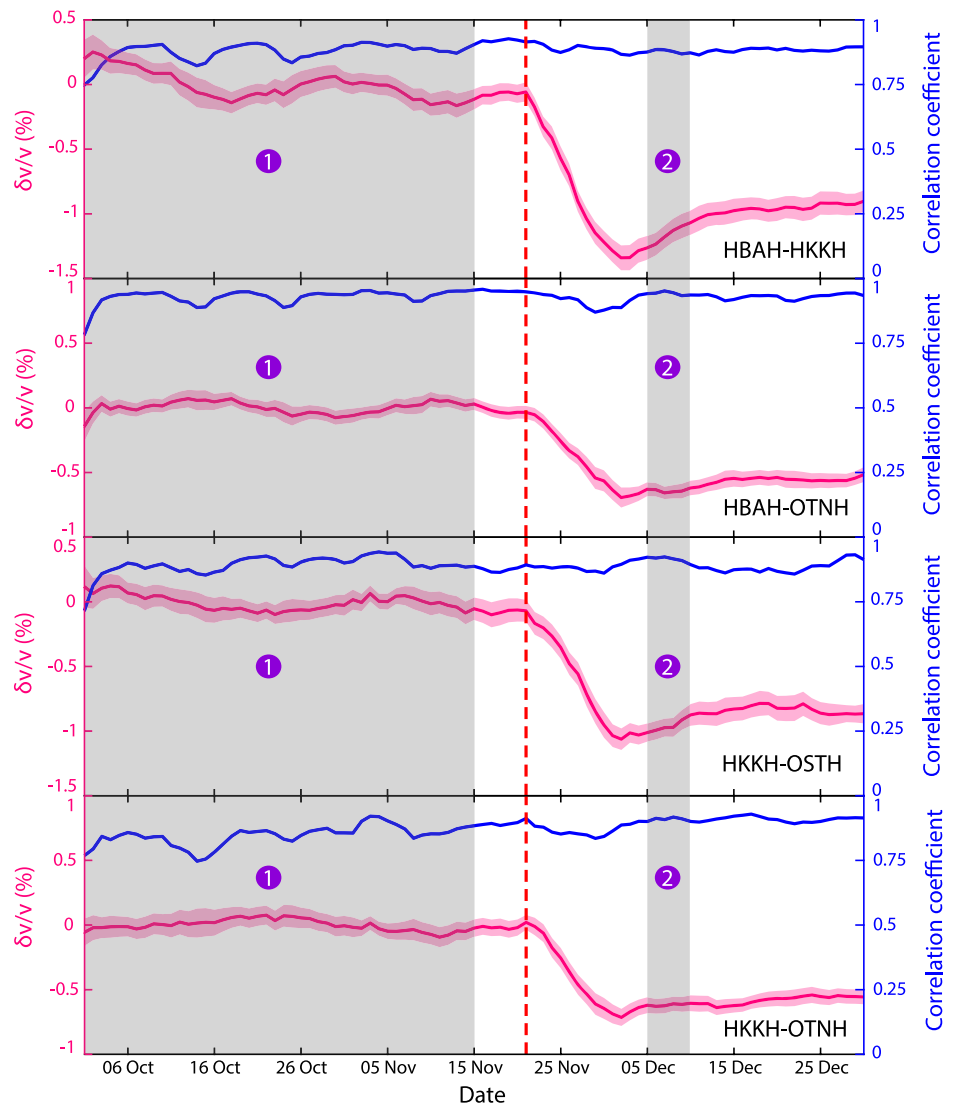
Our analysis covers a 3-month time period bracketing the event origin, from October 1 to December 31 2014, to isolate and characterize the co-seismic component of velocity changes. This choice reflects our primary interest in mapping the spatial distribution of velocity variations associated with the main rupture.

Interferometric synthetic-aperture radar data (InSAR), to infer the surface displacement observed after the mainshock and modeled the coseismic slip distribution, has been used to determine the final slip distribution along the causative fault³². The slip model is associated with a non-planar south-east-dipping fault formed by KF and OTNF faults with a maximum slip patch of about 170 cm located in the shallow, first kilometer, crustal layer in the southern area³². The mainshock, located at 3 km depth, induced an aftershock sequence of about 2500 events occurring at depths shallower than 10 km that lasted until the end of December 2014³³. The analysis of the aftershock distribution unraveled the 3D geometric complexity of the fault surface in detail³⁴. The spatiotemporal evolution of aftershocks reveals a cascading rupture across nine fault segments, highlighting rupture phases, kinematic variations, and stress field changes, aiding fault mapping and earthquake understanding.

For this event, the analysis of the seismic velocity changes using ambient noise interferometry with a station located 26 km from the epicenter revealed a velocity drop of -1.4% below 150 m with partial recovery over four months³⁵. These changes were attributed to dynamic strain from strong ground motion rather than static coseismic deformation, with faster recovery in the upper 150 m linked to initial medium damage. However, as this analysis is based on the auto-correlation of a single station, the spatial variability of velocity changes remains unsolved. Expanding the analysis to multiple stations is essential to reconstruct the full spatial complexity of velocity changes, extending to depths of several kilometers where seismicity occurs. By focusing on the M_w 6.2 Nagano earthquake, characterized by a complex fault surface rupture, this study aims to better understand how a moderate magnitude earthquake spatially affects the medium properties. This contributes to a more comprehensive understanding of how velocity variations relate to rupture processes and medium damage under different geological conditions. Moreover, direct field observations of velocity reductions in areas where the fault ruptured the surface remain rare³⁶. This makes our case particularly valuable, as it provides in-situ evidence of fault zone damage, allowing a more direct connection to fault mechanics than laboratory or simulated data.

To build on this approach and address the spatial variability of velocity changes, we extracted velocity variations using the ambient noise cross-correlation technique applied to continuous waveform records from 27 Hi-net seismic stations³⁷ distributed across the mainshock area, at distances

Fig. 2 | Velocity variations versus time. Velocity variations for several station pairs HBAH-HKKH, HBAH-OTNH, HKKH-OSTH, and HKKH-OTNH calculated in the frequency band [0.1–1 Hz] with a temporal resolution of one day. The blue curve is the correlation coefficient related to each estimated $\frac{\delta v}{v}$ value. Light pink shading corresponds to the error in the $\frac{\delta v}{v}$ measurement. Red dashed lines indicate the M_w 6.2 earthquake occurrence time. The reference period (1) and the time interval used to analyze the velocity variations (2) in this study are represented by transparent gray boxes.



ranging from 5 to 40 km from the epicenter. Using 351 station-pair cross-correlation functions, together with auto-correlation and single-station cross-correlation functions for amplitude validation³⁸, we resolved a spatial pattern of velocity variations in both the horizontal plane and depth.

We interpreted the mechanism responsible for the observed velocity variations by comparing their spatial extent with the mainshock final slip distribution along the primary fault^{39,40}, which is related to the spatial distribution of coseismic fault displacement, and to the peak ground acceleration (PGA) field, that illustrates the intensity of ground shaking and stress changes in the medium^{41,42}.

A seismic velocity drop was found within the top kilometer where the M_w 6.2 Northern Nagano earthquake rupture reached the surface. This localized decrease overlaps with surface rupture, high-slip faults, and maximum PGA, indicating fault zone damage and near-surface shaking from the mainshock as the main causes. While, deeper aftershock-induced damage appears minimal. These results underscore fault zone weakening and shaking-induced damage as major post-earthquake drivers.

Results

In Fig. 2 we show the velocity variations calculated for station pairs HBAH-HKKH, HBAH-OTNH, HKKH-OSTH, and HKKH-OTNH (see positions in Fig. 1) with a temporal resolution of one day and the corresponding maximum correlation coefficient, estimated using the stretching method (see Methods section). The time series of the velocity variations estimated

from the auto-correlation and single station cross-correlation functions of the station HKKH and OMYH are shown in SI (see Fig. S1 in Supplementary Information). From 1 October 2014 to the date of the mainshock occurrence (22 November), no velocity variation is observed for any of the station pairs. However, starting from 23 November, a decrease in the $\frac{\delta v}{v}$ of 0.5–1.3% can be observed for the station pairs, and the single station, located closest to the earthquake sequence epicenters (Fig. 2 and Fig. S1 in SI). To analyze the velocity changes located near the mainshock epicenter, we defined the reference time interval before (from 1 October to 15 November 2014; period “1” in Fig. 2), for which the velocity variations are small (smaller than two times the standard deviation), and the time interval after the main drop of $\frac{\delta v}{v}$ (5–10 December 2014; period “2” in Fig. 2) for the station pairs and the single station closer to the mainshock epicentral area. Since the effective temporal resolution is determined by the 10-day moving stack of daily NCFs used to stabilize the correlation coefficient, our results are insensitive to short-lived velocity changes ranging from hours to a few days immediately following the mainshock (see Methods). We observed that the velocity decrease is much larger for short offset station pairs and single station located closer to the mainshock epicenter, up to –1.3% within the first 5 km, as compared to more distant ones, either considering the midpoint of the station pair (Fig. 3) or the closest-epicenter station in the pair (Fig. S2 in Supplementary Information). These observations suggest a spatial-temporal correlation of the velocity perturbations and the mainshock location. Moreover, the amplitude of the velocity drop is similar

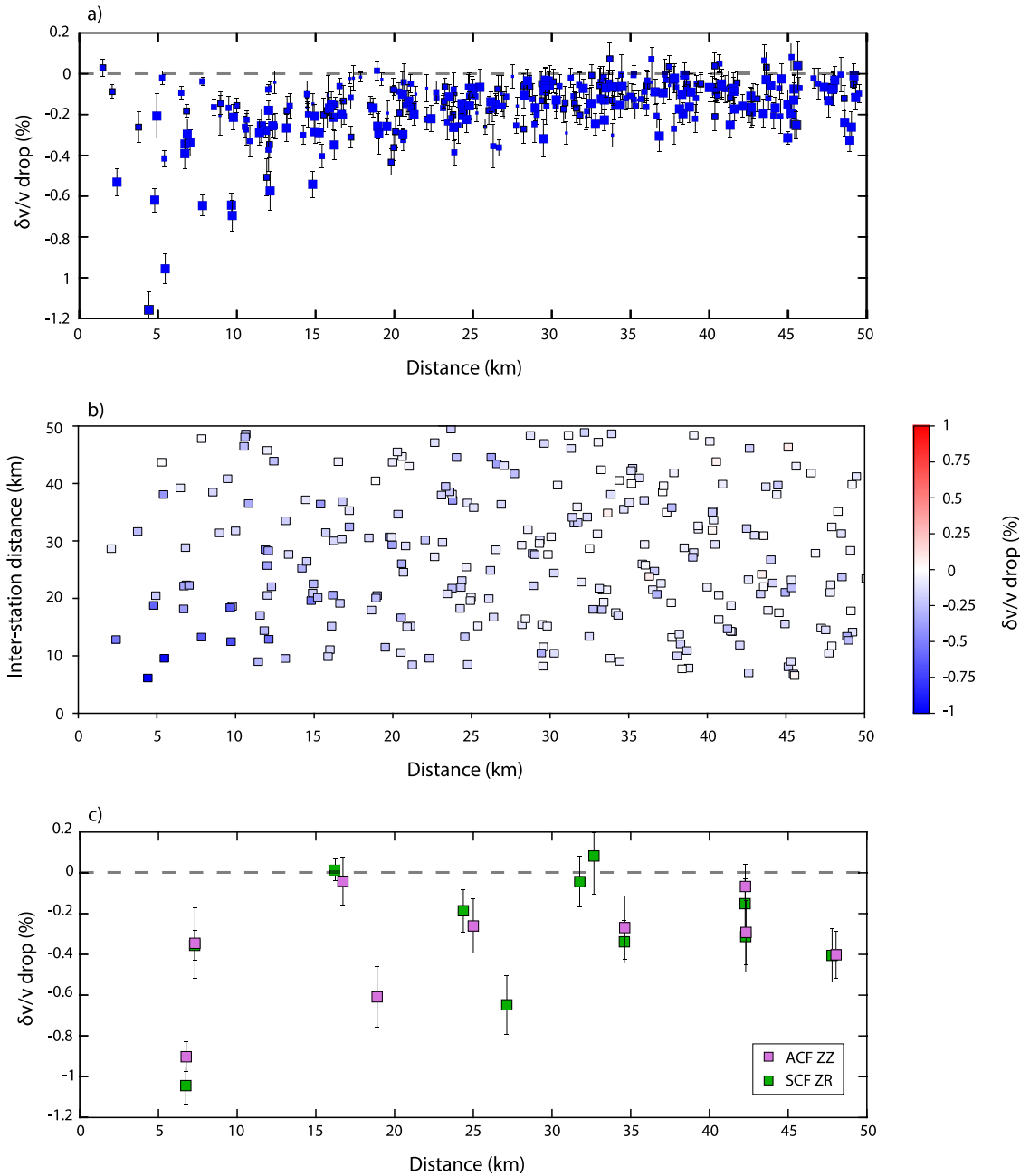


Fig. 3 | Observed velocity variations versus distance. **a** Velocity variations with error bars for the time interval (5–10 December 2014) with respect to the reference period, for any of the station pairs, as a function of the distance between the M_w 6.2 earthquake location and the midpoint of the station pair. **b** Inter-station distance and

velocity variations as a function of the distance between the M_w 6.2 earthquake location and the mid-point of the station pair. **c** Same as (a) for the auto-correlation functions (ACF) and single station cross-correlation functions (SCF).

between the cross-correlation of station pairs and the auto-correlation of single stations. To better quantify this spatial correlation, we located the velocity changes in the horizontal plane by considering the geometry of the sensitivity kernel and further estimated the depth distribution of the velocity perturbations (see Methods).

Figure 4 shows the mapped velocity perturbations, calculated in the frequency band [0.1–1 Hz] and for the time period 5–10 December 2014. Amplitudes changes are determined as the difference between values measured in the reference time period. A velocity decrease is observed between these two intervals and affects the broad epicentral area of the M_w 6.2 earthquake. The restitution index calculated from the resolution matrix (see Methods) during the inversion indicates that the velocity perturbations are well retrieved in most of the crustal volume (see Fig. 4).

The spatial distribution of velocity variations shows that the velocity decrease extends over an area of approximately 20 km around the mainshock, with a maximum reduction of -0.5% observed a few kilometers from the epicenter, between stations HBAH and HKKH (pink diamond in Fig. 4).

Figure 5 shows the depth distribution of the velocity perturbations calculated for three station pairs (HBAH-HKKH, HBAH-OTNH, and HKKH-OSTH), located near the maximum velocity decrease, from 5 to 10 December. The amplitude of velocity variations after the mainshock, observed for these station pairs, decreases with increasing frequency band of the analysis (Fig. 5d–f). The velocity variations, estimated in the frequency band [0.1–1 Hz], affect the first kilometer of depth (Fig. 5a–c) and the restitution index calculation confirms that the velocity variations estimated

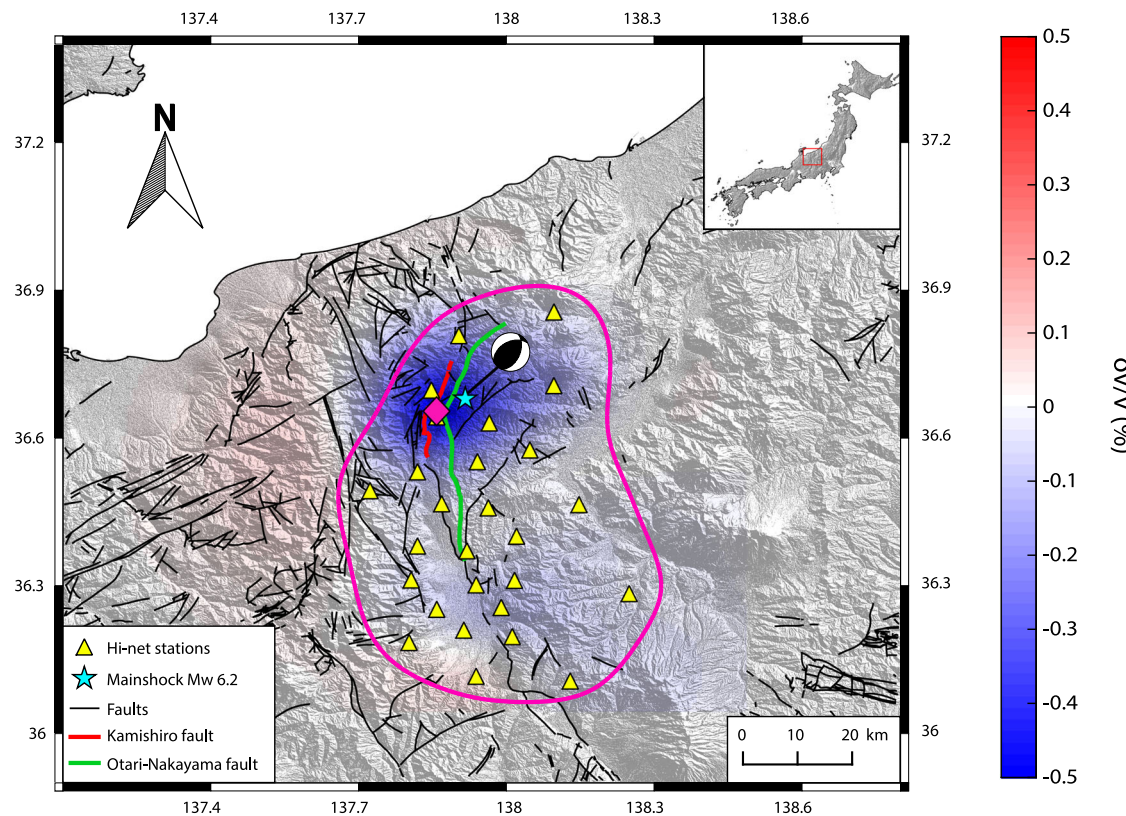


Fig. 4 | Map of velocity perturbations for the time interval 5–10 December 2014, with respect to the reference period, in the frequency band [0.1–1 Hz]. The pink contour represents the iso-value 0.8 of the restitution index. The velocity is well recovered inside this contour. The pink diamond indicates the position of the

maximum velocity decrease of about -0.5% . The red and green lines on the map correspond to the fault traces at the surface of the Kamishiro fault and the Otari–Nakayama fault respectively. Faults and geological units from GSJ–AIST (2025, CC BY 4.0); topography from GSI DEM10B (OGL–Japan).

in the shallow 2 km crustal layer are reliable. Deeper perturbations have no detectable influence on velocities in the frequency band [0.1–1 Hz].

Discussion

The detection and mapping of the velocity changes using ambient noise interferometry, show that the M_w 6.2 2014 Northern Nagano earthquake rupture induced a seismic velocity decrease between 0.5 and 1.3% revealed by the stations within 10 km epicentral distance (Figs. 2, 3 and Figs. S1–S2 in SI). The consistency between the amplitude of velocity drops retrieved from cross-correlation and auto-correlation, coherently with other works^{20,38}, confirms the robustness of our estimates and supports the interpretation that the observed velocity changes are not biased by the choice of the correlation function. The horizontal location and the depth distribution of the velocity perturbations suggest that the M_w 6.2 earthquake induced the estimated velocity changes in the shallow 2 km thick crustal layer, to which we are sensitive in the studied frequency band, in the area where the mainshock rupture reached the surface (Figs. 4, 5). The decrease in seismic velocity in the fault embedding crustal volume after a moderate size earthquake has also been observed in previous studies in other seismic regions^{5,18,20,25,43}. For the 2014 Nagano earthquake, the average seismic velocity decrease is of about 1.4% within the first hundreds of meters of depth³⁵.

Several causes have been proposed to explain the occurrence of velocity perturbations after a large earthquake, such as the static-stress transfer in the fault zone^{14,23,44–47}, changes in ground water near surface or fluid activity in the shallow crust^{11–13,24}, near-surface damage from ground shaking^{5,18,43,48–50}, and damage to the crust in the vicinity of the mainshock fault zone rupture^{25,51–56}.

Static-stress induced velocity changes are related to the closing (dominant compression, seismic velocity increases) and opening (dominant

dilatation, seismic velocity decreases) of pre-existing cracks isotropically distributed under the action of dominant stress changes^{23,44,56}. During the investigated period, no velocity increase was observed through seismic noise interferometry analysis in the region affected by the 2014 Nagano earthquake sequence. Like other studies^{5,56}, we base on this observation to exclude static-stress changes as the main cause of the post-event velocity perturbations.

An alternative hypothesis is that near-surface damage due to strong ground shaking can cause the velocity decrease following large earthquakes^{5,18,25,43,50}. The nonlinear response of the very shallow material of the crust under the action of dynamic strain is generally associated with a widespread decrease of velocity whose amplitude is spatially correlated with the strong ground shaking level^{5,18}. We investigated the spatial distribution of the PGA of the mainshock measured from 24 strong motion records from the M_w 6.2 Northern Nagano earthquake of the Kiban Kyoshin network (KiK-net) operated by NIED³⁷. The maximum PGA, observed at the nearest-to-epicenter station (NGN005) (see Fig. 6), is 0.6 g. While most of the other stations measured a PGA equal to lower than 0.1 g, station NGN002 at a distance of 29 km recorded a PGA of 0.36 g (see Fig. 6). Station NGN002 is at the border of the high-resolution volume for our noise interferometry analysis (see Fig. 6) so that velocity variations in the volume around this station were not retrievable with sufficient accuracy. We also calculated the PGA of the mainshock recorded at Hi-net stations to compare with the seismic velocity drop derived from auto-correlation and single-station cross-correlation functions (Fig. S3 in Supplementary Information). Restricting the analysis to velocity variations with a maximum error of 0.25 and a minimum correlation coefficient of 0.5, we found a clear spatial correlation between areas of high PGA and the largest seismic velocity drops near the mainshock location (see Fig. S3 in Supplementary Information). Despite the resolution limit of the Hi-net network, and the poor spatial

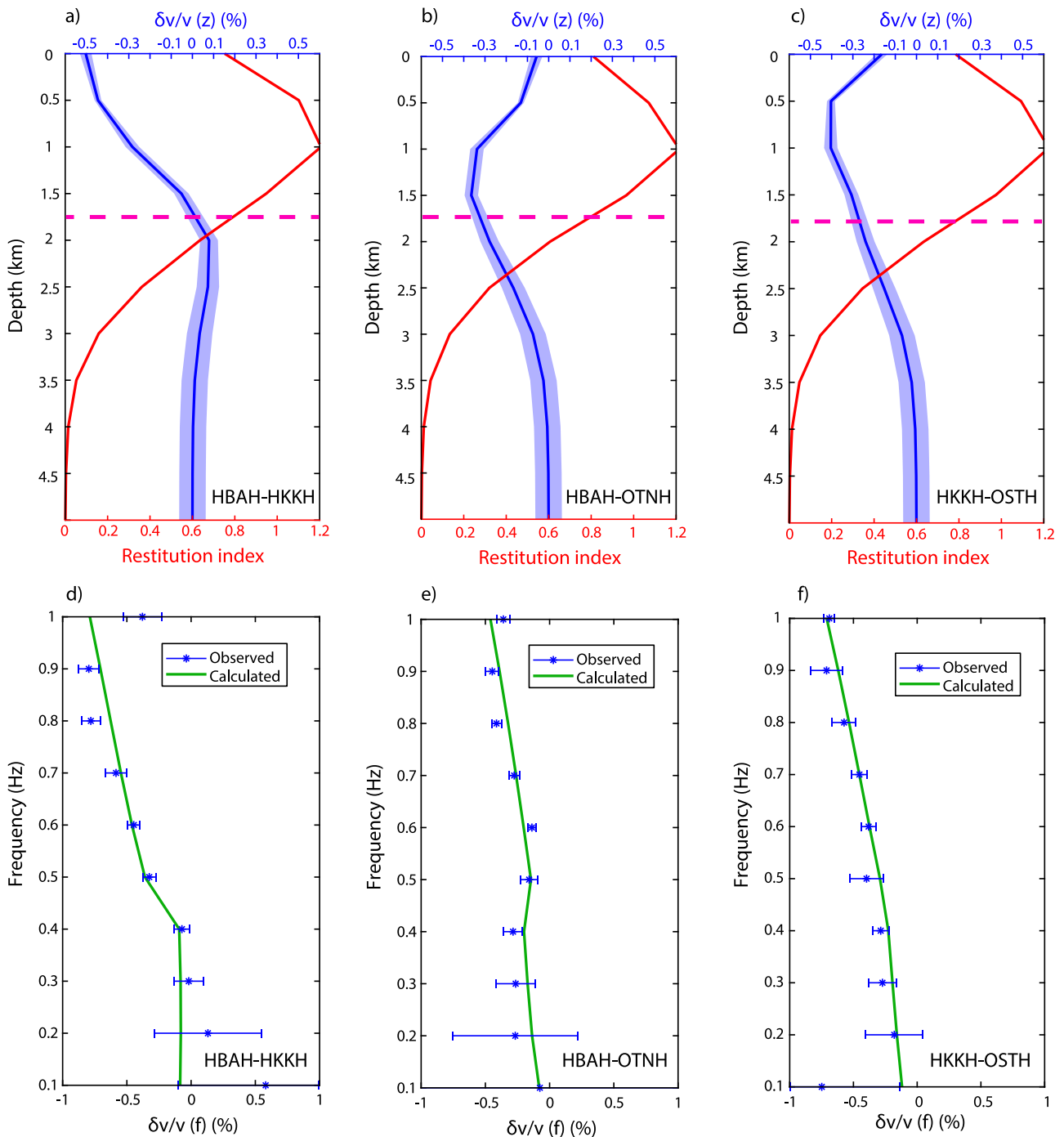


Fig. 5 | Distribution of the velocity variations as a function of depth for 5–10 December 2014. Velocity variations (blue line) and restitution index (red line) as a function of depth for the station pair **a** HBAH-HKKH, **b** HBAH-OTNH, and **c** HKKH-OSTH. Calculated (green line) and observed (blue stars with error bars) velocity perturbations, as a function of frequency for the station pair **d** HBAH-

HKKH, **e** HBAH-OTNH, and **f** HKKH-OSTH. Light blue shading corresponds to the error in the $\frac{\delta v}{v}$ measurement. The pink dashed line corresponds to the depth below which the restitution index is lower than 0.8, so that the velocity perturbations are poorly retrieved.

coverage of the KiK-net network, in the region of the earthquake sequence the maximum PGA region well correlates spatially with the area of the maximum seismic velocity change, thus supporting the hypothesis that strong ground shaking is a possible cause of the observed post-event velocity variations.

Velocity variations induced by damage of the crust within the fault rupture volume have been observed as a consequence of large earthquakes in other regions^{25,51–57}. The mechanical damage process refers to weakening of the earthquake fault surrounding medium, which induces, in the damaged

volume, a decrease in the effective shear modulus and therefore of the seismic velocity. Large earthquakes produce off-fault damage distributed in a volume around the fault rupture that can affect the geometry and the rheology of the fault zone. The final slip distribution of the mainshock rupture model³² shows a maximum slip, of 170 cm, located west of the mainshock epicenter within the first kilometer of the crustal layer (Fig. 7).

Laboratory studies investigating fault weakening and acoustic properties under controlled slip conditions provide a valuable mechanical framework for interpreting our field-based observations. High-velocity friction

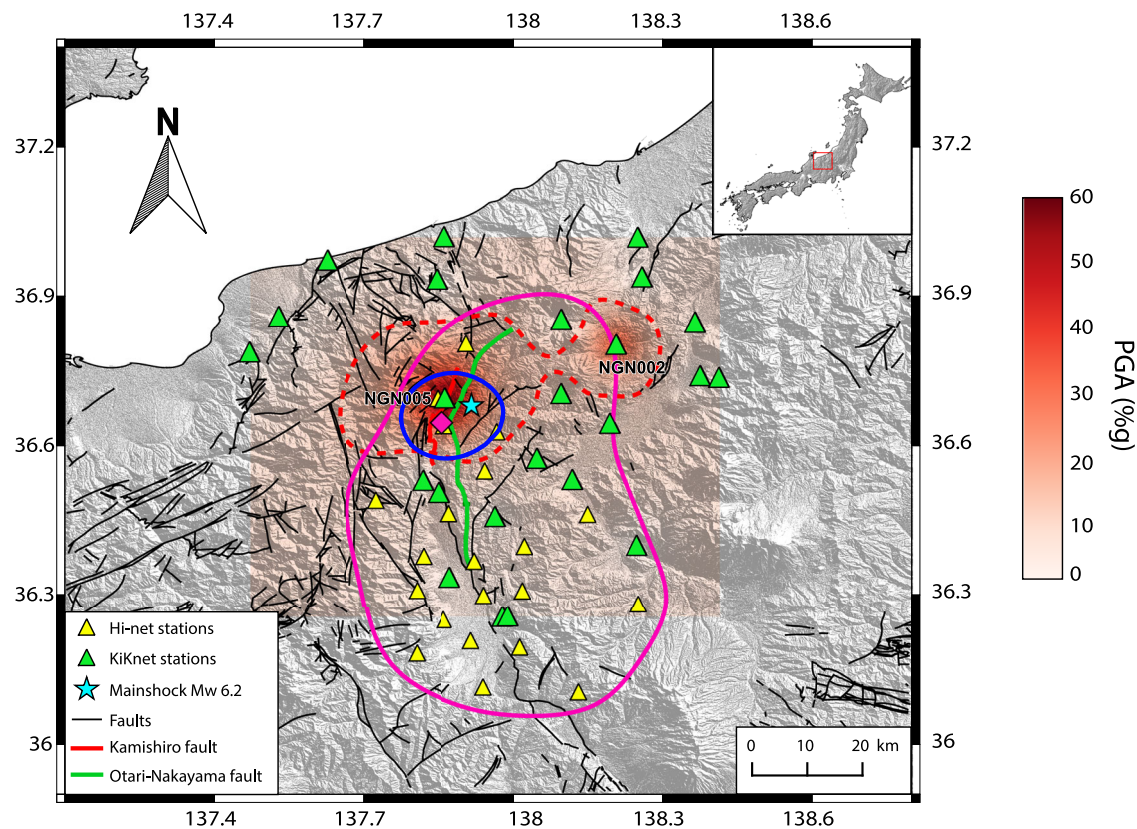


Fig. 6 | Map view showing the distribution of the peak ground acceleration (PGA) measured on the mainshock. The pink contour is the isovalue 0.8 of the restitution index indicating that the velocity is well recovered inside this contour. The pink diamond indicates the position of the maximum velocity decrease of about -0.5% . The blue contour is the isovalue of velocity decrease of about -0.3% . The red dashed

contour is the isovalue of PGA of about 0.1 g. The red and green lines on the map correspond to the fault traces at the surface of the Kamishiro fault and the Otari-Nakayama fault respectively. Faults and geological units from GSJ-AIST (2025, CC BY 4.0); topography from GSI DEM10B (OGL-Japan).

experiments have shown that coseismic slip induces rapid asperity breakage and gouge comminution, leading to a permanent reduction in elastic stiffness and frictional strength^{58–60}. These microscale processes plausibly account for the observed velocity drop in regions of intense slip and surface rupture. Complementary experiments tracking acoustic transmissivity during complex slip histories demonstrate a robust correlation between transmissivity and frictional strength, indicating that seismic wave velocities can act as sensitive proxies for the evolving mechanical state of fault interfaces^{61,62}. In addition, a well-documented transition from velocity-strengthening to velocity-weakening behavior at steady-state has been observed in both rock and natural fault gouge samples, and is thought to result from changes in contact structure and slip rate⁶³. Together, these findings support the interpretation that the observed velocity reduction reflects irreversible structural damage induced by dynamic rupture and strong ground motion in the shallow crust.

While our analysis focuses on the coseismic and early post-seismic velocity changes occurring within three months of the mainshock, we acknowledge that longer-term recovery processes, such as elastic re-equilibration or healing, may develop over extended timescales. As such, our results do not capture the full temporal evolution of post-seismic changes, which should be addressed in future work.

The spatial distribution of the velocity perturbations obtained from the contribution of numerous pairs of stations, provides a location of the maximum velocity drop closely matching the region where the rupture reached the surface and 1 km from the high slip patch. The high sensitivity depth range, where the velocity variations are estimated, includes the fault region where the maximum slip has been detected (Fig. 7). The close agreement between the spatial distribution of maximum velocity drop, the region of observed surface fault breakages and the region of maximum slip at

1 km depth, supports the hypothesis that the observed velocity variations are associated with the wide fault zone damage caused by the mainshock rupture. Damage induced by aftershock sequence could also contribute to the observed changes. However, if aftershocks are large and active, incremental damage from aftershocks could cause additional velocity reduction^{8,23} and slow recovery speed. Another observation that lead us to reduce the contribution of aftershock to observed velocity drop is that more than 90% of the aftershock activity occurs at depths greater than about 2 km^{33,34} (see Fig. S4 in Supplementary Information). Since the seismic noise is not sensitive to deeper perturbations in the studied frequency band [0.1–1 Hz] (see Fig. 5 and Fig. S4 in Supplementary Information), the contribution of induced incremental damage by deeper aftershock ruptures is likely minimal.

We applied ambient noise interferometry to measure post-seismic velocity variations in the region affected by the 2014 M_w 6.2 Nagano earthquake. By mapping the distribution of these changes and comparing it with the mainshock's coseismic slip and the PGA distribution, our results suggest that velocity reduction in the first kilometers of depth is primarily linked to damage at shallow depth from the mainshock rupture. Both strong near-surface ground motions and fault zone damage play a role in the observed damage, to which we are sensitive. However, the limited coverage of strong-motion stations constrains our understanding to distinguish between these two mechanisms.

Our results highlight the necessity of accurately locating velocity perturbations both laterally and at depth to assess their spatial correlation with the mainshock. This is crucial for a more comprehensive understanding of the mechanisms driving velocity variations. Additionally, integrating these observations with other geophysical parameters sensitive to the mechanical state of the medium, such as peak ground acceleration and stress changes, is

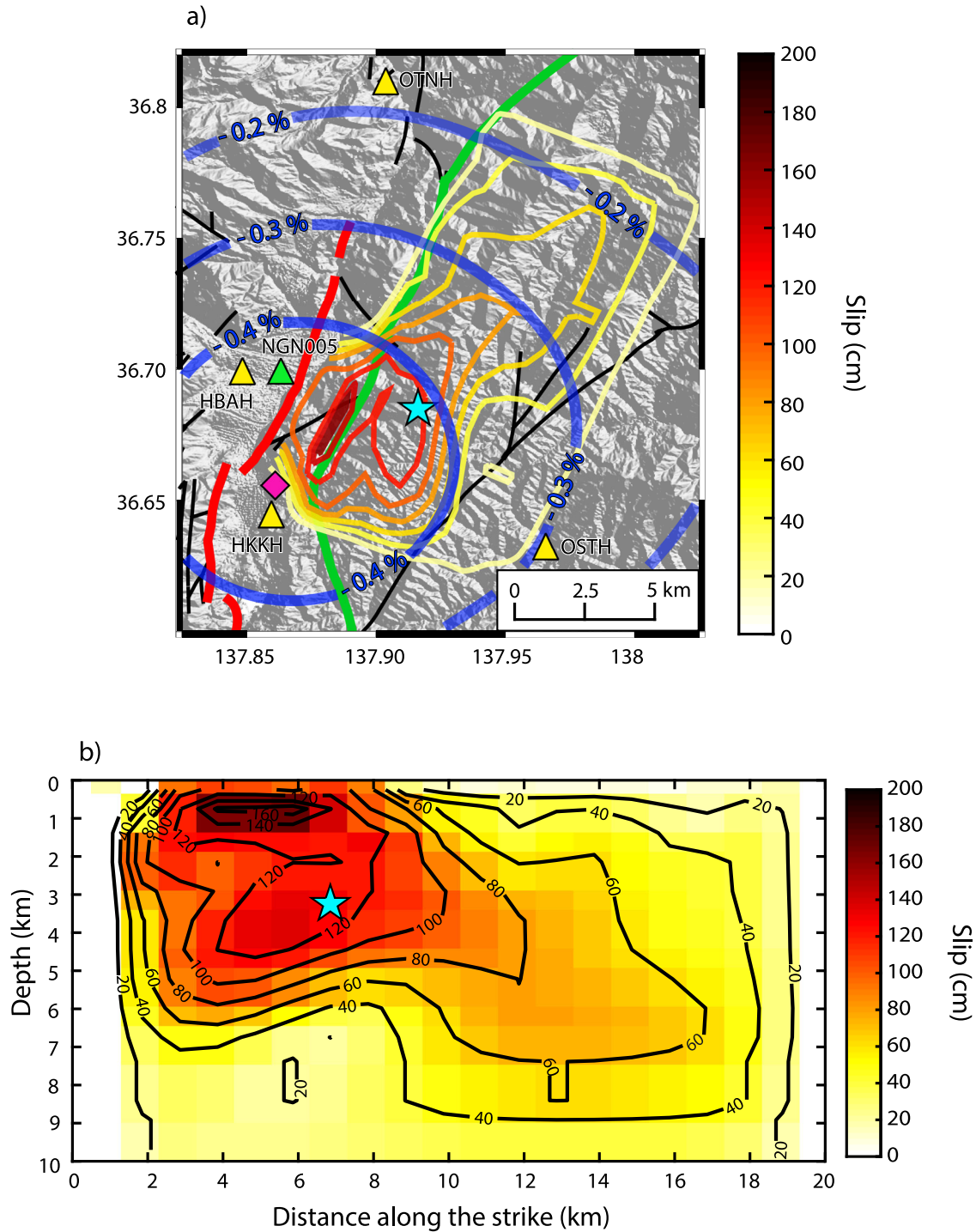


Fig. 7 | Comparison of velocity decrease with slip model. **a** Map view showing a projection of the contour slip model³². The blue contour represents isovalues of velocity decrease mapped on Fig. 4. The red and green lines on the map correspond to the fault traces at the surface of the Kamishiro fault and the Otari–Nakayama fault

respectively. The area is displayed with a white square on Fig. 1. **b** Projection at depth of the slip model³². The black lines indicate the contour of the slip along the fault. The cyan star corresponds to the mainshock. Faults and geological units from GSJ–AIST (2025, CC BY 4.0); topography from GSI DEM10B (OGL–Japan).

key to identifying the processes responsible for the observed velocity changes.

Methods

Data and calculation of noise cross-correlation functions

The data used in this study is the continuous seismic waveforms recorded from 1st October to 31 December 2014 of 27 short period stations of the permanent network Hi-net operated by the National Research Institute for Earth Science and Disaster Resilience (NIED) and the Japan Meteorological

Agency³⁷ (JMA) (see Fig. 1). The inter-station distance range is from 6 km (HBAH–HKKH) to 70 km (MAZH–OTNH). To calculate the noise cross-correlation functions (NCF) the vertical component seismic records were filtered between 0.1 Hz and 1 Hz, split into 1800 s duration segments, and clipped to 3 root mean square to reduce the effects of seismic events before applying the frequency domain normalization. NCFs between 351 station pairs were calculated using the MSNoise software⁶⁴ and linearly stacked over a day (indicating that the daily NCF is the average of the NCF of all 1800 s duration windows in the day). The daily auto-correlation and the single

station cross-correlation functions were computed following the same procedure. The correlogram obtained for station pair HBAH-HKHH (Fig. S5 in Supplementary Information) shows the stability of the daily NCFs over the entire period and confirms the ability to extract NCFs with coherent arrivals in the coda.

The amplitude of the coda waves decreases exponentially over time (Fig. S5 in Supplementary Information). To determine the end of the coda, we plotted the logarithm of the amplitude envelope and identified the decrease until delays of about 100 s (Fig. S5 in Supplementary Information). As the beginning of the coda is influenced by the inter-station distance, we defined a dynamic coda window to extract velocity variations depending on the velocity of the slowest ballistic waves. By assuming a velocity of 1 km/s, we observed the beginning of the coda window with higher delay for larger inter-station distance and the coda starts at a delay lower than 100 s (Fig. S6 in Supplementary Information). We used 30 s window duration and a minimum lag of 10 s to consider the most energetic coda waves (Fig. S7 in Supplementary Information).

Velocity variations in time

Velocity variations, $\frac{\delta v}{v}$, are estimated by comparing travel time changes in the coda of daily NCFs and the reference NCF using stretching method^{24,65}. Assuming a homogenous velocity changes distribution, the stretching coefficient ϵ gives a weighted average of the velocity variations $\frac{\delta v}{v}$ following:

$$\epsilon = \frac{\delta t}{t} = \frac{-\delta v}{v} \quad (1)$$

The primary condition to obtain reliable velocity variations is the relative stability of the background noise structure, while a full reconstruction of the Green's function is not necessary⁶⁶. The minimum correlation coefficient between the reference NCF and the daily NCFs in the coda window (defined in the previous section) is of about 0.5 and the maximum uncertainty⁶⁷ of the $\frac{\delta v}{v}$ of about 0.25. In order to smooth the $\frac{\delta v}{v}$ curves and increase the correlation coefficient, the reference NCF is defined by stacking the daily NCFs over the entire period (from 1st October to 31 December 2014). Different moving stack lengths over the preceding days were tested (2-days, 5-days, 10-days, and 20-days; see Fig. S8 in Supplementary Information) to determine the appropriate size in order to identify how clearly the velocity changes were resolved and the related correlation coefficients estimated by the stretching method. We determined that a moving stack of the NCFs over the 10 preceding days shows clear velocity changes with a stable correlation coefficient above 0.8 over the entire time period (Fig. S8 in Supplementary Information).

Locating velocity perturbations

Coda waves are a combination of bulk and surface waves in a heterogeneous medium due to conversions between these two types of waves. Early time lag coda waves mostly probably propagate as surface waves and are sensitive to shallow velocity changes, while later time lag coda waves mostly propagate as bulk waves with deeper sensitivity⁷. The apparent velocity variations decrease for shallow perturbations and increase for deeper perturbations with increasing time lag in the coda⁷. Here below, several arguments to justify that surface waves are dominant in the coda waves we explored to extract the velocity variations:

1. We selected some station pairs located close to the M_w 6.2 Nagano earthquake and we observe that the drop of velocity decrease with increasing time lag in the coda of the NCF, that is coherent with the velocity changes close to the surface due to the dominance of surface waves sensitivity in the early coda wave (see Fig. S9 in Supplementary Information). Then decrease of the velocity drop could be related to the extension of the sampled medium by the coda waves to regions where the velocity perturbations could be smaller.
2. There is an increase in the absolute velocity variations with frequency (see Fig. 5d–f) which is consistent with the assumption that surface waves are dominant in the coda waves we explored.

3. The wavelengths corresponding to the studied frequency band [0.1–1 Hz] are larger than the estimated depth of the perturbations. Surface waves are sensitive to these shallow perturbations.

By assuming that the coda of the NCF is dominated by multi-scattered surface waves propagating along a random walk process in a 2D medium⁶⁸, the horizontal distribution of the velocity perturbations can be modeled by solving the following equation as a linear inverse problem^{7,8,18,69–72}:

$$\frac{\delta v}{v}(t) = \frac{-\delta t(t)}{t} = \frac{1}{t} \int_S K(s_1, s_2, x_0, t) \frac{\delta v}{v}(x_0) dS(x_0) \quad (2)$$

where $\frac{\delta t}{t}(t)$ is the relative travel time change of a diffusive wavefield. $\frac{\delta v}{v}(t)$ are the velocity variations in time calculated for different station pairs. $\frac{\delta v}{v}(x_0)$ is the spatial distribution of the velocity variations produced in the medium at the position x_0 . $K(s_1, s_2, x_0, t)$ is the kernel sensitivity that represents the distribution of travel time of the multi-scattered waves propagating from the source location s_1 to the receiver location s_2 after visiting the perturbation at x_0 . The solution of the linearized inverse problem⁷³, described in Eq. 2, is given by:

$$m = C_m G^t (G C_m G^t + C_d)^{-1} d \quad (3)$$

where d is the data vector which is the estimated velocity variations at all the station pairs. G is the matrix of kernels sensitivity. m is the model of spatial distribution of the velocity perturbations $\frac{\delta v}{v}(x_0)$. C_d is the covariance matrix of the data. C_m is the covariance matrix of the model such as:

$$C_m(x_i, x_j) = \left(\sigma_m \frac{\lambda_0}{\lambda_m} \right)^2 \exp \left(\frac{-(x_i - x_j)^2}{\lambda^2} \right) \quad (4)$$

where σ_m is the a priori standard deviation of the model, λ_0 is the grid interval, λ is a correlation length, and x_i and x_j are the position vectors of two cells of the model. The L-curve criterion⁷⁴ is used to defined λ and σ_m . With a grid spacing λ_0 of about 1 km, we used a correlation length λ of 10 km and the a priori standard deviation of the model σ_m of about 0.015. To estimate the resolution of the spatial distribution model of the velocity variations, we used the restitution index⁷⁵ that is calculated by summing the elements of the rows of the resolution matrix⁷⁶: $R = C_m G^t (G C_m G^t + C_d)^{-1} G$. Value close to one indicates well recovered velocity variations in the corresponding element of the model as well.

Assuming that coda waves are dominated by Rayleigh waves, we can estimate the depth of the perturbations by using the sensitivity of the velocity perturbations to deeper sources at low frequency then at high frequency. The depth distribution of the velocity perturbation $\frac{\delta v}{v}(z)$ can be modeled by inverting the following equation as a linear least square inversion problem^{8,18}:

$$\frac{\delta v}{v}(f) = \int_z K_d(z, f) \frac{\delta v}{v}(z) dz \quad (5)$$

where $\frac{\delta v}{v}(f)$ is the velocity variations estimated for a given station pair for different frequency bands. $K_d(z, f)$ is the kernel sensitivity defined as the derivative of the Rayleigh phase velocity with respect to the S-wave velocity⁷⁷ (see Fig. S10 in Supplementary Information):

$$K_d(z, f) = \frac{\delta c}{\delta v_s}(z, f) \quad (6)$$

We computed the velocity variations at different frequency bands with a frequency spacing of 0.1 Hz and a constant width of 0.2 Hz to sample properly the function $\frac{\delta v}{v}(f)$.

Data availability

The continuous seismic records (Hi-net data) analyzed in this paper are available via <https://doi.org/10.17598/NIED.0003>. The NCFs used in this study will be available via the Zenodo archive⁷⁸ (<https://doi.org/10.5281/zenodo.17157854>). The Seamless Digital Geological Map of Japan (version 2, 1:200,000; faults and geological units) in Figs. 1, 4, 6, and 7 is provided by the Geological Survey of Japan, AIST, under the Creative Commons Attribution 4.0 International License (CC BY 4.0) (<https://gbank.gsj.jp/seamless/>). The 10 m digital elevation model (DEM10B) in Figs. 1, 4, 6, and 7 is distributed by the Geospatial Information Authority of Japan (GSI) under the Open Government License – Japan (<https://fgd.gsi.go.jp/download/menu.php>).

Code availability

The continuous waveforms were processed to compute the NCFs using the code MSNoise (available via <http://www.msnoise.org>). Maps were prepared using QGIS (QGIS Development Team, 2025. QGIS Geographic Information System. Open Source Geospatial Foundation Project. <http://qgis.org>).

Received: 12 February 2025; Accepted: 7 October 2025;

Published online: 19 November 2025

References

- Brenguier, F. et al. Postseismic relaxation along the San Andreas fault at Parkfield from continuous seismological observations. *Science* **321**, 1478–1481 (2008).
- Niu, F., Silver, P. G., Daley, T. M., Cheng, X. & Majer, E. L. Preseismic velocity changes observed from active source monitoring at the Parkfield SAFOD drill site. *Nature* **454**, 204–208 (2008).
- Shapiro, N. M. & Campillo, M. Emergence of broadband Rayleigh waves from correlations of the ambient seismic noise. *Geophys. Res. Lett.* **31**, L07614 (2004).
- Rivet, D. et al. Seismic evidence of nonlinear crustal deformation during a large slow slip event in Mexico. *Geophys. Res. Lett.* **38**, L08308 (2011).
- Madley, M. et al. Velocity changes around the Kaikōura earthquake ruptures from ambient noise cross-correlations. *Geophys. J. Int.* **229**, 1357–1371 (2022).
- Brenguier, F. et al. Towards forecasting volcanic eruptions using seismic noise. *Nat. Geosci.* **1**, 126–130 (2008).
- Obermann, A., Planès, T., Larose, E. & Campillo, M. Imaging preeruptive and coeruptive structural and mechanical changes of a volcano with ambient seismic noise. *J. Geophys. Res. Solid Earth* **118**, 6285–6294 (2013).
- Muzellec, T., Lesage, P., Caudron, C. & Got, J. L. Migration of mechanical perturbations estimated by seismic coda wave interferometry during the 2018 pre-eruptive period at Kilauea Volcano, Hawaii. *J. Geophys. Res. Solid Earth* **128**, e2022JB026224 (2023).
- Meier, U., Shapiro, N. M. & Brenguier, F. Detecting seasonal variations in seismic velocities within Los Angeles basin from correlations of ambient seismic noise. *Geophys. J. Int.* **181**, 985–996 (2010).
- Hillers, G., Ben-Zion, Y., Campillo, M. & Zigone, D. Seasonal variations of seismic velocities in the San Jacinto fault area observed with ambient seismic noise. *Geophys. J. Int.* **202**, 920–932 (2015).
- Tarantino, S. et al. Non-linear elasticity, earthquake triggering and seasonal hydrological forcing along the Irpinia fault, Southern Italy. *Nat. Commun.* **15**, 9821 (2024).
- Yates, A. S. et al. Seasonal snow cycles and their possible influence on seismic velocity changes and eruptive activity at Ruapehu volcano, New Zealand. *J. Geophys. Res. Solid Earth* **129**, e2024JB029568 (2024).
- Kramer, R. et al. Identifying large vulnerable water reservoirs using passive seismic monitoring. *Earth Planet. Sci. Lett.* **653**, 119223 (2025).
- Xu, Z. J. & Song, X. Temporal changes of surface wave velocity associated with major Sumatra earthquakes from ambient noise correlation. *Proc. Natl. Acad. Sci. USA* **106**, 14207–14212 (2009).
- Froment, B., Campillo, M., Chen, J. H. & Liu, Q. Y. Deformation at depth associated with the 12 May 2008 Mw 7.9 Wenchuan earthquake from seismic ambient noise monitoring. *Geophys. Res. Lett.* **40**, 78–82 (2013).
- Takano, T., Nishimura, T. & Nakahara, H. Seismic velocity changes concentrated at the shallow structure as inferred from correlation analyses of ambient noise during volcano deformation at Izu-Oshima, Japan. *J. Geophys. Res. Solid Earth* **122**, 6721–6736 (2017).
- Wu, S. M. et al. Spatiotemporal seismic structure variations associated with the 2018 Kilauea eruption based on temporary dense geophone arrays. *Geophys. Res. Lett.* **47**, e2019GL086668 (2020).
- Lesage, P., Reyes-Dávila, G. & Arámbula-Mendoza, R. Large tectonic earthquakes induce sharp temporary decreases in seismic velocity in Volcán de Colima, Mexico. *J. Geophys. Res. Solid Earth* **119**, 4360–4376 (2014).
- Taira, T. A., Brenguier, F. & Kong, Q. Ambient noise-based monitoring of seismic velocity changes associated with the 2014 Mw 6.0 South Napa earthquake. *Geophys. Res. Lett.* **42**, 6997–7004 (2015).
- Hobiger, M., Wegler, U., Shiomi, K. & Nakahara, H. Coseismic and postseismic elastic wave velocity variations caused by the 2008 Iwate-Miyagi Nairiku earthquake, Japan. *J. Geophys. Res. Solid Earth* **117**, B09313 (2012).
- Boschelli, J., Moschetti, M. P. & Sens-Schönfelder, C. Temporal seismic velocity variations: recovery following from the 2019 Mw 7.1 Ridgecrest, California earthquake. *J. Geophys. Res. Solid Earth* **126**, e2020JB021465 (2021).
- Poli, P., Marguin, V., Wang, Q., d'Agostino, N. & Johnson, P. Seasonal and coseismic velocity variation in the region of L'Aquila from single station measurements and implications for crustal rheology. *J. Geophys. Res. Solid Earth* **125**, e2019JB019316 (2020).
- Rubinstein, J. L. & Beroza, G. C. Evidence for widespread nonlinear strong ground motion in the Mw 6.9 Loma Prieta earthquake. *Bull. Seismol. Soc. Am.* **94**, 1595–1608 (2004).
- Sens-Schönfelder, C. & Wegler, U. Passive image interferometry and seasonal variations of seismic velocities at Merapi Volcano, Indonesia. *Geophys. Res. Lett.* **33**, L21302 (2006).
- Nimiya, H., Ikeda, T. & Tsuji, T. Spatial and temporal seismic velocity changes on Kyushu Island during the 2016 Kumamoto earthquake. *Sci. Adv.* **3**, e1700813 (2017).
- Bonilla, L. F., Guéguen, P. & Ben-Zion, Y. Monitoring coseismic temporal changes of shallow material during strong ground motion with interferometry and autocorrelation. *Bull. Seismol. Soc. Am.* **109**, 187–198 (2019).
- Nakata, N. & Snieder, R. Estimating near-surface shear wave velocities in Japan by applying seismic interferometry to KiK-net data. *J. Geophys. Res.* **117**, B01308 (2012).
- Clements, T. & Denolle, M. A. Tracking groundwater levels using the ambient seismic field. *Geophys. Res. Lett.* **45**, 6459–6465 (2018).
- Japan Meteorological Agency, Monthly report on earthquakes and volcanoes in Japan. <http://www.data.jma.go.jp/svd/eqev/data/gaikyo/monthly/201411/201411monthly.pdf> (2014).
- National Research Institute for Earth Science and Disaster Resilience, NIED seismic moment tensor catalogue. National Research Institute for Earth Science and Disaster Resilience. (available online from: <http://www.fnet.bosai.go.jp/event/joho.php?>) (2014).
- Okada, S., Ishimura, D., Niwa, Y. & Toda, S. The first surface-rupturing earthquake in 20 years on a HERP active fault is not characteristic: the 2014 Mw 6.2 Nagano Event along the Northern Itoigawa-Shizuoka Tectonic Line. *Seismol. Res. Lett.* **86**, 1287–1300 (2015).
- Kobayashi, T., Morishita, Y. & Yarah, H. SAR-revealed slip partitioning on a bending fault plane for the 2014 Northern Nagano earthquake at

- the northern Itoigawa–Shizuoka tectonic line. *Tectonophysics* **733**, 85–99 (2018).
33. Panayotopoulos, Y. et al. Seismological evidence of an active footwall shortcut thrust in the Northern Itoigawa–Shizuoka Tectonic Line derived by the aftershock sequence of the 2014 M 6.7 Northern Nagano earthquake. *Tectonophysics* **679**, 15–28 (2016).
 34. Muzellec, T., De Landro, G., Camanni, G., Adinolfi, G. M. & Zollo, A. The complex 4D multi-segmented rupture of the 2014 Mw 6.2 Northern Nagano Earthquake revealed by high-precision aftershock locations. *Tectonophysics* **898**, 230641 (2025).
 35. Sawazaki, K., Saito, T., Ueno, T. & Shiomi, K. Estimation of seismic velocity changes at different depths associated with the 2014 Northern Nagano Prefecture earthquake, Japan (MW 6.2) by joint interferometric analysis of NIED Hi-net and KiK-net records. *Prog. Earth Planet. Sci.* **3**, 1–15 (2016).
 36. Hillers, G. et al. Seismic velocity change patterns along the San Jacinto fault zone following the 2010 M7.2 El Mayor-Cucapah and M5.4 Collins Valley earthquakes. *J. Geophys. Res. Solid Earth* **124**, 7171–7192 (2019).
 37. National Research Institute for Earth Science and Disaster Resilience, NIED K-NET, KiK-net, National Research Institute for Earth Science and Disaster Resilience, <https://doi.org/10.17598/NIED.0004> (2019).
 38. Hobiger, M., Wegler, U., Shiomi, K. & Nakahara, H. Single-station cross-correlation analysis of ambient seismic noise: application to stations in the surroundings of the 2008 Iwate-Miyagi Nairiku earthquake. *Geophys. J. Int.* **198**, 90–109 (2014).
 39. Heaton, T. H. Evidence for and implications of self-healing pulses of slip in earthquake rupture. *Phys. Earth Planet. Inter.* **64**, 1–20 (1990).
 40. Ji, C., Wald, D. J. & Helmberger, D. V. Source description of the 1999 Hector Mine, California, earthquake; Part I: wavelet domain inversion theory and resolution analysis. *Bull. Seismol. Soc. Am.* **92**, 1192–1207 (2002).
 41. Wald, D., Wald, L., Worden, B., & Goltz, J. ShakeMap, a tool for earthquake response. *Fact Sheet* (2003).
 42. Kanamori, H. & Jennings, P. C. Determination of local magnitude, M_L , from strong-motion accelerograms. *Bull. Seismol. Soc. Am.* **84**, 713–720 (1994).
 43. Chaves, E. J. & Schwartz, S. Y. Monitoring transient changes within overpressured regions of subduction zones using ambient seismic noise. *Sci. Adv.* **2**, e1501289 (2016).
 44. Poupinet, G., Ellsworth, W. L. & Frechet, J. Monitoring velocity variations in the crust using earthquake doublets: an application to the Calaveras Fault, California. *J. Geophys. Res. Solid Earth* **89**, 5719–5731 (1984).
 45. Ratdomopurbo, A. & Poupinet, G. Monitoring a temporal change of seismic velocity in a volcano: application to the 1992 eruption of Mt. Merapi (Indonesia). *Geophys. Res. Lett.* **22**, 775–778 (1995).
 46. Dodge, D. A. & Beroza, G. C. Source array analysis of coda waves near the 1989 Loma Prieta, California, mainshock: implications for the mechanism of coseismic velocity changes. *J. Geophys. Res. Solid Earth* **102**, 24437–24458 (1997).
 47. Nishimura, T. et al. Temporal changes in seismic velocity of the crust around Iwate volcano, Japan, as inferred from analyses of repeated active seismic experiment data from 1998 to 2003. *Earth Planets Space* **57**, 491–505 (2005).
 48. Guyer, R. A. & Johnson, P. A. Nonlinear mesoscopic elasticity: evidence for a new class of materials. *Phys. today* **52**, 30–36 (1999).
 49. Johnson, P. A. & Jia, X. Nonlinear dynamics, granular media and dynamic earthquake triggering. *Nature* **437**, 871–874 (2005).
 50. Sawazaki, K., Sato, H., Nakahara, H. & Nishimura, T. Time-lapse changes of seismic velocity in the shallow ground caused by strong ground motion shock of the 2000 Western-Tottori earthquake, Japan, as revealed from coda deconvolution analysis. *Bull. Seismol. Soc. Am.* **99**, 352–366 (2009).
 51. Li, Y. G., Vidale, J. E., Aki, K., Xu, F. & Burdette, T. Evidence of shallow fault zone strengthening after the 1992 M 7.5 Landers, California, earthquake. *Science* **279**, 217–219 (1998).
 52. Li, Y. G., Vidale, J. E., Day, S. M., Oglesby, D. D. & Cochran, E. Postseismic fault healing on the rupture zone of the 1999 M 7.1 Hector Mine, California, earthquake. *Bull. Seismol. Soc. Am.* **93**, 854–869 (2003).
 53. Li, Y. G., Chen, P., Cochran, E. S., Vidale, J. E. & Burdette, T. Seismic evidence for rock damage and healing on the San Andreas fault associated with the 2004 M 6.0 Parkfield earthquake. *Bull. Seismol. Soc. Am.* **96**, S349–S363 (2006).
 54. Vidale, J. E. & Li, Y. G. Damage to the shallow Landers fault from the nearby Hector Mine earthquake. *Nature* **421**, 524–526 (2003).
 55. Rubinstein, J. L., Uchida, N. & Beroza, G. C. Seismic velocity reductions caused by the 2003 Tokachi-Oki earthquake. *J. Geophys. Res. Solid Earth* **112**, B05315 (2007).
 56. Wegler, U., Nakahara, H., Sens-Schönfelder, C., Korn, M. & Shiomi, K. Sudden drop of seismic velocity after the 2004 Mw 6.6 mid-Niigata earthquake, Japan, observed with Passive Image Interferometry. *J. Geophys. Res. Solid Earth* **114**, B06305 (2009).
 57. Liu, Z., Huang, J., He, P. & Qi, J. Ambient noise monitoring of seismic velocity around the Longmenshan fault zone from 10 years of continuous observation. *J. Geophys. Res. Solid Earth* **123**, 8979–8994 (2018).
 58. Yamashita, F., Fukuyama, E. & Mizoguchi, K. Probing the slip-weakening mechanism of earthquakes with electrical conductivity: rapid transition from asperity contact to gouge comminution. *Geophys. Res. Lett.* **41**, 341–347 (2014).
 59. Im, K., Elsworth, D. & Wang, C. Cyclic permeability evolution during repose then reactivation of fractures and faults. *J. Geophys. Res. Solid Earth* **124**, 4492–4506 (2019).
 60. Barbot, S. A rate-, state-, and temperature-dependent friction law with competing healing mechanisms. *J. Geophys. Res. Solid Earth* **127**, e2022JB025106 (2022).
 61. Nagata, K., Nakatani, M. & Yoshida, S. Monitoring frictional strength with acoustic wave transmission. *Geophys. Res. Lett.* **35**, L06310 (2008).
 62. Shreedharan, S., Rivière, J., Bhattacharya, P. & Marone, C. Frictional state evolution during normal stress perturbations probed with ultrasonic waves. *J. Geophys. Res. Solid Earth* **124**, 5469–5491 (2019).
 63. Nie, S. & Barbot, S. Velocity and temperature dependence of steady-state friction of natural gouge controlled by competing healing mechanisms. *Geophys. Res. Lett.* **51**, e2023GL106485 (2024).
 64. Lecocq, T., Caudron, C. & Brenguier, F. MSNoise, a python package for monitoring seismic velocity changes using ambient seismic noise. *Seismol. Res. Lett.* **85**, 715–726 (2014).
 65. Lobkis, O. I. & Weaver, R. L. Coda-wave interferometry in finite solids: recovery of P-to-S conversion rates in an elastodynamic billiard. *Phys. Rev. Lett.* **90**, 254302 (2003).
 66. Hadziioannou, C., Larose, E., Coutant, O., Roux, P. & Campillo, M. Stability of monitoring weak changes in multiply scattering media with ambient noise correlation: laboratory experiments. *J. Acoust. Soc. Am.* **125**, 3688–3695 (2009).
 67. Weaver, R. L., Hadziioannou, C., Larose, E. & Campillo, M. On the precision of noise correlation interferometry. *Geophys. J. Int.* **185**, 1384–1392 (2011).
 68. Pacheco, C. & Snieder, R. Time-lapse travel time change of multiply scattered acoustic waves. *J. Acoust. Soc. Am.* **118**, 1300–1310 (2005).
 69. Larose, E., Planes, T., Rossetto, V. & Margerin, L. Locating a small change in a multiple scattering environment. *Appl. Phys. Lett.* **96**, 204101 (2010).
 70. Froment, B. *Utilisation du bruit sismique ambiant dans le suivi temporel de structures géologiques* (PhD dissertation, University of Grenoble, France, 2011).

71. Planès, T. *Imagerie de chargements locaux en régime de diffusion multiple* (PhD dissertation, University of Grenoble, France, 2013).
72. Machacca-Puma, R., Lesage, P., Larose, E., Lacroix, P. & Ancasí-Figueroa, R. M. Detection of pre-eruptive seismic velocity variations at an andesitic volcano using ambient noise correlation on 3-component stations: Ubinas volcano, Peru, 2014. *J. Volcanol. Geotherm. Res.* **381**, 83–100 (2019).
73. Tarantola, A. & Valette, B. Generalized nonlinear inverse problems solved using the least squares criterion. *Rev. Geophys.* **20**, 219–232 (1982).
74. Hansen, P. C. Analysis of discrete ill-posed problems by means of the L-curve. *SIAM Rev.* **34**, 561–580 (1992).
75. Vergely, J. L., Valette, B., Lallement, R. & Raimond, S. Spatial distribution of interstellar dust in the sun’s vicinity-comparison with neutral sodium-bearing gas. *Astron. Astrophys.* **518**, A31 (2010).
76. Backus, G. E. & Gilbert, J. F. Numerical applications of a formalism for geophysical inverse problems. *Geophys. J. Int.* **13**, 247–276 (1967).
77. Herrmann, R. B. Computer programs in seismology, Source inversion, St. Louis Univ., St. Louis, Mo (2004).
78. Muzellec, T., De Landro, G. & Zollo, A. Unraveling earthquake-induced damage: insights from ambient noise interferometry of the 2014 Mw 6.2 northern nagano earthquake: noise cross-correlation functions [Data set]. Zenodo. <https://doi.org/10.5281/zenodo.17157854> (2025).

Acknowledgements

We thank the Geological Survey of Japan, AIST, for the Seamless Digital Geological Map of Japan (CC BY 4.0) and the Geospatial Information Authority of Japan for the DEM10B digital elevation data (Open Government License – Japan). This work has received financial support by the “Multi-Risk sciEence for resilienT commUnities undeR a changiNg climate” (RETURN) project, funded by the European Union’s NextGenerationEU and the Italian Ministry of University and Research (MUR) under the National Recovery and Resilience Plan (NRRP; Code PE0000005). We would like to thank the Editor, Luc Illien, and the anonymous reviewer for their comments and suggestions that allowed us to improve the manuscript.

Author contributions

Conceptualization: T.M. and G.D.L. Formal Analysis: T.M. Interpretation: T.M., G.D.L., and A.Z. Visualization: T.M. Funding acquisition: A.Z. Supervision: A.Z. and G.D.L. Writing – original draft: T.M. and G.D.L., Writing – review & editing: T.M., G.D.L., and A.Z.

Competing interests

The authors declare no competing interests.

Additional information

Supplementary information The online version contains supplementary material available at <https://doi.org/10.1038/s43247-025-02890-1>.

Correspondence and requests for materials should be addressed to Grazia De Landro.

Peer review information *Communications Earth and Environment* thanks Luc Illien and the other, anonymous, reviewer(s) for their contribution to the peer review of this work. Primary Handling Editors: Adriana Paluszny and Joe Aslin. A peer review file is available.

Reprints and permissions information is available at <http://www.nature.com/reprints>

Publisher’s note Springer Nature remains neutral with regard to jurisdictional claims in published maps and institutional affiliations.

Open Access This article is licensed under a Creative Commons Attribution-NonCommercial-NoDerivatives 4.0 International License, which permits any non-commercial use, sharing, distribution and reproduction in any medium or format, as long as you give appropriate credit to the original author(s) and the source, provide a link to the Creative Commons licence, and indicate if you modified the licensed material. You do not have permission under this licence to share adapted material derived from this article or parts of it. The images or other third party material in this article are included in the article’s Creative Commons licence, unless indicated otherwise in a credit line to the material. If material is not included in the article’s Creative Commons licence and your intended use is not permitted by statutory regulation or exceeds the permitted use, you will need to obtain permission directly from the copyright holder. To view a copy of this licence, visit <http://creativecommons.org/licenses/by-nc-nd/4.0/>.

© The Author(s) 2025